

The electrical conductivity tensor of β -Ga₂O₃ analyzed by van der Pauw measurements: Inherent anisotropy, off-diagonal element, and the impact of grain boundaries

Christian Golz, Vanesa Hortelano, Fariba Hatami, and W. Ted Masselink
Department of Physics, Humboldt-Universität zu Berlin, Newton-Str. 15, D-12489 Berlin, Germany.

Zbigniew Galazka
Leibniz-Institut für Kristallzüchtung, Max-Born-Str. 2, 12489 Berlin, Germany.

Oliver Bierwagen
*Paul-Drude-Institut für Festkörperelektronik, Leibniz-Institut im
 Forschungsverbund Berlin e.V., Hausvogteiplatz 5–7, D-10117 Berlin, Germany.**
 (Dated: March 13, 2019)

The semiconducting oxide β -Gallium Oxide (β -Ga₂O₃) possesses a monoclinic unit cell whose low symmetry generally leads to anisotropic physical properties. For example, its electrical conductivity is generally described by a polar symmetrical tensor of second rank consisting of four independent components. Using van der Pauw measurements in a well-defined square geometry on differently-oriented high-quality bulk samples and the comparison to finite element simulations we precisely determine the ratio of all elements of the β -Ga₂O₃ 3-dimensional electrical conductivity tensor. Despite the structural anisotropy a nearly isotropic conductivity at and above room temperature was found with the principal conductivities deviating from each other by less than 6 % and the off-diagonal element being ≈ 3 % of the diagonal ones. Analysis of the temperature dependence of the anisotropy and mobility of differently doped samples allows us to compare the anisotropy for dominant phonon-scattering to that for dominant ionized-impurity scattering. For both scattering mechanisms, the conductivities along the a and b -direction agree within 2 %. In contrast, the conductivity along c -direction amounts to $0.96\times$ and up to $1.12\times$ that along the b -direction for phonon and ionized impurity scattering, respectively. The determined transport anisotropies are larger than the theoretically predicted effective mass anisotropy, suggesting slightly anisotropic scattering mechanisms. We demonstrate that significantly higher anisotropies can be caused by oriented extended structural defects in the form of low-angle grain boundaries for which we determined energy barriers of multiple 10 meV.

PACS numbers:

I. INTRODUCTION

β -Ga₂O₃, the thermodynamically stable polymorph of solid Ga₂O₃, is a promising material for several applications such as high power electronics[1, 2] and deep UV photo detectors[2, 3], and it can be used for high-temperature gas sensors[4]. β -Ga₂O₃ has a monoclinic lattice structure, which corresponds to the C2/m-space group with lattice parameters of $a = 12.23$ Å, $b = 3.04$ Å, and $c = 5.80$ Å and an angle of 103.7° between a and c -axis[5]. Due to this angle, the basis vectors of the unit cell, a and c , are not orthogonal to the (100) and (001) planes in β -Ga₂O₃. The low symmetry of the unit cell is prone to result in anisotropic physical properties.

Notable anisotropies in β -Ga₂O₃ have been found in the thermal conductivity [6–8] and the dielectric function by the polarization-dependent refractive index [9] and fundamental onset of optical absorption [9–11]. In addition, slight anisotropies of the high-frequency and static dielectric constant of β -Ga₂O₃ have been reported by theory and experiment[12–16]. The conductivity anisotropy is given by the ratio of the electrical conductivity in two different defined directions. The same holds true for the mobility tensor $\bar{\mu}$ as

$\bar{\sigma} = en\bar{\mu}$, as the charge carrier density n and electronic charge e are scalars.

For electronic device applications such as transistors, a mobility anisotropy would translate into an increased performance of the devices for a certain orientation compared to the crystallographic directions. As shown in Tab. I, quite contradictory experimental values on the conductivity anisotropy can be found in literature, whereas no estimate has been reported so far on the off-diagonal element of conductivity. Reported conductivity anisotropies are ranging from 17 times higher conductivity for the b -direction compared to the c direction [10], over the same mobility in a and b direction and 1.2 times higher conductivity in c -direction [20] to a negligible anisotropy [17], where no direction was favored for transport. In metal-oxide field effect transistors (MOSFETs), a 10% larger channel mobility in the a^* direction compared to the c direction has been observed[21]. Using ellipsometry, the same mobility in a and b , but only half the mobility in c -direction has been measured [14]. In combination with an external magnetic field, the same method, termed optical Hall effect, has yielded rather isotropic mobilities (within $\approx 10\%$)[22].

As the mobility depends on the effective mass m^* and scattering time τ , $\mu = \frac{e\tau}{m^*}$, its anisotropy is determined by the anisotropy of m^* and τ . Surprisingly, first-principles calculations from several groups using different methods arrive at a fairly isotropic effective electron mass [12, 25–27] with

*Electronic address: bierwagen@pdi-berlin.de

Table I: Overview of the literature on transport anisotropies and associated methods in β -Ga₂O₃. The anisotropy ‘‘Aniso.’’ is the ‘‘Quantity’’ in direction ‘‘Dir.1’’ divided by that in ‘‘Dir.2’’ at room-temperature electron concentration ‘‘ $n@RT$ ’’. Directions a, b, c are parallel to the a, b, c axes of the unit cell, and a^*, c^* are parallel to the (100), (001) surface normals. ‘‘n\’’ denotes ‘‘not specified’’. #The samples used for different transport directions had different electron concentrations. *The anisotropy of less than 1.1 for σ (line 3) was calculated from a van der Pauw resistance anisotropy ratio of less than 1.3 given in Ref. [17] using the conversion into conductivity anisotropy elaborated in Ref. [18].

Quantity	Method	Dir.1	Dir.2	Aniso.	$n(\text{cm}^{-3}) @RT$	Ref.
σ	4-probe	b	c	17 (extrinsic?)	5.2×10^{18}	[10]
σ	van der Pauw	b	c	2 (twins)	$> 10^{18}$	[19]
σ	van der Pauw	all	all	<1.1 *	$5 \times 10^{16} - 5 \times 10^{17}$	[17]
μ	Hall bar	c	a, b	1.2 #	$4 \times 10^{17}, 7 \times 10^{17}, 9 \times 10^{17}$	[20]
μ	MOSFET channel	a^*	c	1.1	3×10^{17}	[21]
μ	ellipsometry	a, b	c^*	2	3.5×10^{18}	[14]
μ	optical Hall	all	all	<1.1	$4 \times 10^{18}, 6 \times 10^{18}$	[22]
μ_{PLOS}	theory	c^*	a	1.18 to 1.40	10^{17} to 10^{20}	[23]
μ_{PLOS}	theory	a	b	0.85 to 0.78	10^{17} to 10^{20}	[23]
μ_{PLOS}	theory	c^*	b	1.01 to 1.09	10^{17} to 10^{20}	[23]
μ_{IIS}	theory	n\	n\	estimated <1.4	-	[23]
μ_{PLOS}	theory	c^*	b	0.64 to 0.92	5×10^{17} to 10^{19}	[24]
μ_{IIS}	theory	any	any	assumed 1	5×10^{17} to 10^{19}	[24]
$\mu_{PLOS+IIS}$	theory	c^*	b	0.69 to 0.92	5×10^{17} to 10^{19}	[24]
m^*	optical Hall	all	all	<1.1	$4 \times 10^{18}, 6 \times 10^{18}$	[22]
m^*	theory	all	all	<1.05	-	[12, 25–27]

anisotropies typically below 1.05, which is confirmed by experimental data of the effective mass using optical Hall effect measurements[22].

The scattering time is related to the dominant scattering mechanism, polar longitudinal optical-phonon scattering (PLOS) and ionized impurity scattering (IIS).[23, 24, 28] At and above room temperature, the mobility is limited by PLOS[23, 28], whereas IIS is dominating at high impurity- or point-defect densities (including compensating impurities/point defects) or lower temperatures. Depending on the scattering mechanism the monoclinic symmetry of β -Ga₂O₃ suggests more or less anisotropic scattering times. Hence, the change of dominant scattering mechanism with temperature likely leads to a temperature-dependent anisotropy of the scattering rates. Recent first-principles calculations of the electron mobility limit of β -Ga₂O₃, indeed, suggested a moderate anisotropy with higher mobility in c^* - than in a - or b -direction.[23] In that work, the PLOS-limited mobility (neglecting IIS) in the c^* -direction has been predicted to be up to 9 % and 40 % higher than in the a - and b - direction, respectively, to become more isotropic with decreasing electron concentrations, and anisotropies of up to 1.4 for the IIS-limited mobility were estimated. Another first principles study,[24] predicts for the PLOS-limited mobility opposite trends with a 36 % lower mobility in the c^* - than in the b -direction, which becomes more isotropic with increasing electron concentration, and isotropic IIS.

Besides the intrinsic material properties, samples might be extrinsically anisotropic on the average due to oriented extended defects like grain- and twin boundaries. As an example, Ref. [19] found a room-temperature transport anisotropy as high as 2 in Ga₂O₃(100) thin films containing a high density of incoherent twin boundaries. Likewise, the high anisotropy of 17 from Ref. [10] has been interpreted in terms of extrinsic

causes by Refs. [17, 23].

In this paper we experimentally determine the intrinsic anisotropy and relative magnitude of the off-diagonal element of the conductivity tensor of β -Ga₂O₃ with high accuracy (uncertainty of 2 %) to shed light on the conflicting values of published theoretical and experimental transport anisotropy. The extracted conductivity is surprisingly isotropic and we find large transport anisotropies to be extrinsically caused by extended defects.

II. SAMPLES AND METHOD

A. Samples

To largely rule-out the extrinsic effect of extended defects on transport anisotropy, semiconducting bulk substrates were chosen as sample material with highest structural quality available. Square shaped $5 \times 5 \text{ mm}^2$ (0.5 mm to 0.7 mm thickness) wafers with different orientations, i. e. Czochralski-grown [29] (100) and (001) and edge-defined film fed grown [30] ($\bar{2}01$) (from Tamura Corporation) were investigated in this work. The edges of the squares were oriented along low-index crystallographic directions. The samples are described in Tab. II. The two (1 0 0) and (0 0 1) oriented samples G100a and G001a were prepared from the same boule. To study the impact of extended defects on the transport anisotropy a (1 0 0)-oriented sample containing low angle grain boundaries, G100c, was prepared.

Disk-shaped ohmic contacts of 100 μm to 450 μm diameter close to the corners of the sample were reproducibly defined on the top surface of the samples using shadow masks and photolithography to minimize geometry errors. A distance of the contacts from the sample edges of 700 μm to

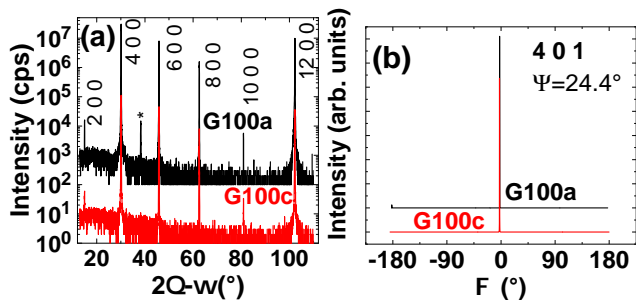


Figure 1: XRD scans to determine the substrate orientation shown exemplarily for samples G100a and G100c. (a) Symmetric on-axis $2\theta - \omega$ scans showing the presence of reflexes, labeled by their Miller indices, only related to the $1\ 0\ 0$ wafer orientation. The peak marked by “*” is related to Au(1 1 1) of the ohmic contact. (b) ϕ -scan of the $4\ 0\ 1$ reflex. The one-fold rotational symmetry indicates single crystalline material without rotational domains or twins.

850 μm was chosen to prevent unintentional contacting the side of the sample by individual contacts. This approach ensures reproducible and well-defined current injection (only through the top surface) by all four contacts to provide a current distribution that can be readily compared to the results of our corresponding finite-element calculations. All contacts were deposited by electron beam evaporation of Ti/Pt/Au (20 nm/20 nm/150 nm), followed by rapid thermal annealing at 480°C for 60 s in N_2 . The Pt layer served as diffusion barrier as deterioration of Ti/Au contacts was observed upon annealing.

The electron densities of the samples were in the range of $8 \times 10^{16}\ \text{cm}^{-3}$ to $6 \times 10^{18}\ \text{cm}^{-3}$ at room temperature.

B. Structural characterization

The crystal quality of the wafers was assessed by X-ray diffraction (XRD) using Cu-K α radiation and a 1 mm detector slit. Wide-range, symmetric, on-axis, $2\theta - \omega$ scans confirmed phase-pure material by the presence of only the $\beta\text{-Ga}_2\text{O}_3$ reflexes belonging to the specified wafer orientation. Figure 1(a) shows an example for the two (100) -oriented wafers G100a and G100c. To detect the potential existence of twins or rotational domains, off-axis XRD peaks were measured by Φ -scans with rotational angle Φ around the surface normal. In these scans, the off-axis diffraction peaks were measured in skew-symmetric geometry with the sample tilted by the angle Ψ . The presence of a single peak in the Φ -scan of the $4\ 0\ 1$ reflex for G100a, b, and c as well as G001a, exemplarily shown in Fig. 1(b) for G100a and G100c, confirms the absence of twins or rotational domains in the $(1\ 0\ 0)$ - and $(0\ 0\ 1)$ oriented samples. Likewise, a one-fold rotational symmetry was confirmed for the $(-2\ 0\ 1)$ oriented sample G-201a by the presence of only one peak in the Φ -scan of the $4\ 0\ 0$ reflex (not shown).

To assess the crystal quality in more detail, ω -rocking curves of the on-axis substrate reflections, sensitive to lattice tilting, were taken for all samples. The low full width at half maximum of these curves below 0.1° , documented in Tab. II,

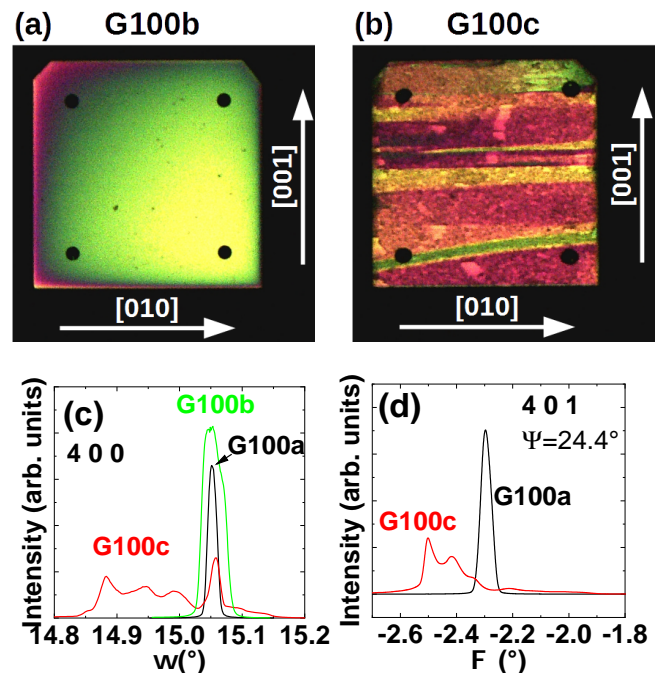


Figure 2: Comparison of (100) -oriented wafers with different structural quality: G100a, b without- and G100c with low angle grain boundaries. (a), (b) Photographs of G100b (a) and G100c (b) placed between two crossed-polarizers with white light illumination from the backside. The crystallographic directions are indicated by white arrows. Horizontal lines in the sample G100c indicate the grain boundaries. No such defects are visible in the sample G100b. The dark dots are the disc-shaped ohmic contacts. (c) XRD ω -rocking curves of the $4\ 0\ 0$ reflex of samples G100a, b and c. (d) XRD detailed Φ -scan of the $4\ 0\ 1$ reflex of G100a and G100c.

confirms the comparably high crystalline quality. The only exception is, sample G100c with a rather broad rocking curve. Figure 2 compares this sample to the other two $(1\ 0\ 0)$ oriented ones. Photographs of the wafers placed between two crossed polarizers with white light illumination from the backside exhibit a comparably homogeneous contrast for G100b shown in Fig. 2(a) but an inhomogeneous contrast with stripes oriented approximately along the $[0\ 1\ 0]$ direction for G100c shown in Fig. 2(b). These stripes represent single crystalline domains that are slightly twisted and tilted with respect to each other as indicated by the multi-peak structure of the rocking curve (Fig. 2(c)) and detailed Φ -scan (Fig. 2(d)), respectively. The inhomogeneous contrast is due to the trichroism of $\beta\text{-Ga}_2\text{O}_3$ resulting in differently colored regions for differently oriented grains.

Hence, all samples can be considered single crystalline except for G100c, which consists of a low number of single crystalline domains with low angle ($<0.3^\circ$) grain boundaries. This sample allows us to investigate the influence of low-angle grain boundaries on the transport properties.

Table II: Overview of the results of the X-Ray diffraction measurements and the properties of the samples: orientation, doping, charge carrier density, and assessed quality. The surface orientation is given by the numbers in the sample name. UID refers to unintentionally doped samples.

Sample name	Orientation; Edges	Doping	Electron density [cm^{-3}]	Quality	XRD ω reflection	ω rocking curve fwhm ($^\circ$)
G100a	(1 0 0); [0 1 0], [0 0 1]	UID	2.5×10^{17}	high	(4 0 0)	0.012
G100b	(1 0 0); [0 1 0], [0 0 1]	UID	8.1×10^{16}	high	(4 0 0)	0.041
G100c	(1 0 0); [0 1 0], [0 0 1]	UID	5.9×10^{17}	low (extended defects)	(4 0 0)	0.180
G001a	(0 0 1); [1 0 0], [0 1 0]	UID	4.3×10^{17}	high	(0 0 2)	0.015
G-201a	($\bar{2}$ 0 1); [1 0 2], [0 1 0]	Sn	5.9×10^{18}	high	($\bar{2}$ 0 1)	0.034

C. Extraction a 2-dimensional conductivity anisotropy by van der Pauw measurements and simulation

In order to investigate the effect of the scattering mechanisms and energy barriers due to low-angle grain boundaries on the conductivity anisotropy, transport measurements were conducted. These measurements were done in van der Pauw geometry (square with four contacts close to the corners) at temperatures between 10 K and 375 K in a closed-cycle helium refrigerator.

Hall measurements were performed in a magnetic field of $B = \pm 0.5$ T oriented perpendicular to the substrate surface. For Hall measurements, two contacts diagonal to each other are used for the current I respectively for measuring the voltage V . Using the two contacts on one edge parallel x of the square sample for applying I and those on the opposite edge for measuring V , the four-terminal resistance along x , R_x , is determined. The same is done for the other two edges (perpendicular to the former ones), which yields R_y . These R_x and R_y are used as described in the original work by van der Pauw to calculate the geometrical average of the anisotropic sheet resistance $R_{ave} = 1/\sqrt{\sigma_x \sigma_y}$. Their ratio $A_{vdP} = R_y/R_x$, can be translated into the conductivity ratio $A = \sigma_x/\sigma_y$ along these axes using finite element methods (FEM) simulations of the current- and voltage distribution for each sample.

We recently described in detail how we used this method for the determination of the transport anisotropy of another semiconducting oxide with anisotropic crystal structure, SnO_2 , [31] and compared the method to the Hall bar geometry [18].

For each sample, geometry details were derived from micrograph images, including the size, position, and shape of the contacts. Using our FEM simulations, the impact of deviations from the ideal van der Pauw geometry for each sample (such as extended size- and position of the contacts away from the sample edges) on measured sheet resistance, its anisotropy, as well as electron concentration n and resulting average mobility $\mu_{ave} = \sqrt{\mu_x \mu_y}$ are correctly accounted for. Examples of a potential distribution resulting from the FEM simulation can be found in Fig. 3. The relation $A(A_{vdP})$ and correction factors for R_{ave} , n , μ_{ave} derived from FEM simulations for the geometries used in this work is summarized in Tabs. III and IV, respectively, as well as Ref. [31].

Obtaining reliable values of A crucially depends on a precisely defined contact geometry as any deviation from a square arrangement by an aspect ratio L_x/L_y of a sample with a length of L_x and L_y impacts the resulting conductivity (or mobility-) anisotropy A by a factor $(L_x/L_y)^2$ [18]. We

Table III: Relation between conductivity anisotropy A and van der Pauw resistance anisotropy A_{vdP} calculated by two-dimensional FEM simulations for square samples with different sizes and positions (offset o_y as shown in Fig. 3) of the disk-shaped contacts. All sizes are relative to the edge length of the square sample.

Contact radius	Distance contact to the edge	Offset of contact position o_y	A	A_{vdP}
all values	all values	0	1	1
0.05	0.2	0.1	1	1.14
0.01	0.01	0	1.1	1.35
0.05	0.1	0	1.1	1.32
0.05	0.2	0	1.1	1.26
0.01	0.01	0	2	9.4
0.05	0.1	0	2	7.7
0.05	0.2	0	2	5.4

Table IV: Correction factors for quantities derived from van der Pauw and Hall measurements for square samples with different sizes and positions (offset o_y as shown in Fig. 3) of the disk-shaped contacts, calculated using two-dimensional FEM simulations. Measured quantities are multiplied by the correction F to obtain the “true” quantities. All sizes are relative to the edge length of the square sample.

Contact radius	Distance contacts to the edge	Offset of contact position o_y	F for R_{ave}	F for n	F for μ_{ave}
0	0	0	1	1	1
0.05	0.1	0	1.01	0.84	1.18
0.05	0.2	0	1.10	0.58	1.57
0.01	0.15	0	1.02	0.80	1.23
0.05	0.2	0.1	1.09	0.60	1.53

tested the accuracy of our experimental technique using several isotropic Si bulk samples, a highly perfect semiconductor, and contact geometry defined by photolithography. The resulting deviations of A from unity was $< 0.7\%$ for each of these samples, which can be seen as the intrinsic geometrical uncertainty of our experiment. A potential experimental artifact that can impact the observed in-plane conductivity anisotropy is the microscopic location of the current injection into the semiconductor under the ohmic contact pad. In our simulations we are assuming current injection along the periphery of the contact. Low electron concentrations and low temperatures can, however, lead to a significant increase of contact resistance and inhomogeneous current injection underneath the contacts (contact freeze-out). For the lithographically defined contacts with diameter of 300(100) μm whose center has a distance of 850(750) μm to nearest sample edges

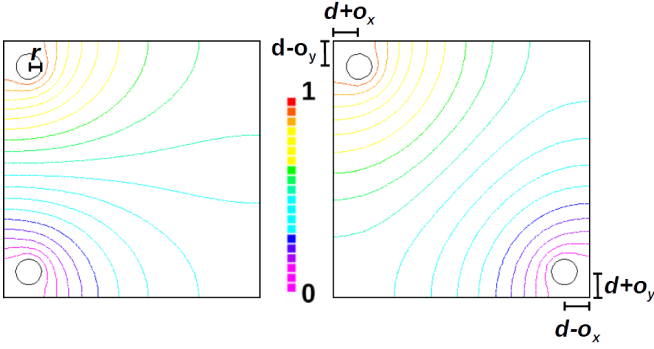


Figure 3: Potential distribution calculated by finite element simulation of a square shaped van der Pauw sample in the configuration used for resistivity anisotropy measurements (left) and Hall-effect measurements (right). r denotes contact radius, d is the distance from the contact to the edge, and o_x and o_y are the offset of the contact position in these directions. In this image, r, d, o_x , and o_y are 0.05, 0.1, 0, and 0 times the sample length, anisotropy $A = 1$ and $B = 0$.

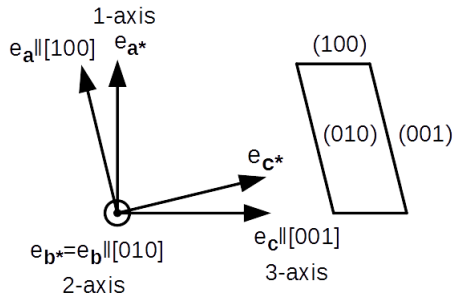


Figure 4: The unit cell of β - Ga_2O_3 projected along the b -axis ($= [010]$ direction). The unit basis vectors along the directions a, b, c and the unit vectors perpendicular to the $(100), (010), (001)$ planes (along $a^*, b^*,$ and c^*) are shown. The 1-axis= e_{a^*} , 2-axis= e_b , and 3-axis= e_c refer to the chosen Cartesian coordinate system to describe the conductivity tensor in this work (a^*bc -system). The angle between a and a^* as well as c and c^* is 13.7° . The vectors a, a^*, c, c^* are in the shown plane and perpendicular to $b = b^*$.

a maximum anisotropy artifact can arise for current injection only at one point on the contact pad that is located e.g. in the horizontal direction towards the outer edge of the sample but in the vertical direction towards the center of the sample. In this extreme case, the maximum apparent van der Pauw anisotropy for isotropic conductivity would be 1.33(1.09), which corresponds to an error for the extracted conductivity anisotropy $\pm 11\%$ ($\pm 3\%$). Experimental comparison of the extracted transport anisotropy of sample G100a and G100b with two different contact sets (300 μm and 100 μm diameter), each, yielded an agreement within 1–2% between the different contact sets, indicating negligible inhomogeneity of current injection underneath the contacts.

D. The 3-dimensional conductivity tensor

Fig. 4 schematically shows the monoclinic unit cell of β - Ga_2O_3 along with the unit basis vectors along a, b, c as well as unit vectors perpendicular to the lowest index planes along a^*, b^*, c^* . The vector representation of physical properties requires an orthonormal system. Two different systems abc^* and a^*bc are chosen by different authors. We will use the a^*bc -system by aligning the 1-axis along (100) surface normal a^* , the 2-axis along b and the 3-axis along the c -axis as indicated in Fig. 4. In this system, the conductivity tensor $\bar{\sigma}$ of β - Ga_2O_3 , that relates electric field \vec{E} and current density \vec{j} by $\vec{j} = \bar{\sigma}\vec{E}$, can be expressed at zero magnetic field as:[32]

$$\bar{\sigma} = \begin{pmatrix} \sigma_{a^*a^*} & 0 & \sigma_{a^*c} \\ 0 & \sigma_{bb} & 0 \\ \sigma_{a^*c} & 0 & \sigma_{cc} \end{pmatrix} \quad (1)$$

where the off-diagonal elements both have the same value σ_{a^*c} . For isotropic materials, the conductivity tensor is a unity matrix times the scalar conductivity value. Different values of the diagonal elements indicate different conductivity values along the axes of the coordinate system. Off-diagonal elements indicate a rotation between the axes of the coordinate system and the directions of minimum and maximum conductivity.

E. Calculation of the 2-dimensional in-plane conductivity tensor

Measurements using the van der Pauw configuration probe the conduction in the plane of the two-dimensional (2D) sample. Thus, a two-dimensional conductivity tensor is required for the analysis and the modeling of the experiment. The non-trivial relation between 2D and 3D tensor for monoclinic materials will be described next for the major available substrate orientations of β - Ga_2O_3 including those used in this work. An overview of these orientations is presented in Fig. 5.

Using the conductivity tensor $\bar{\sigma}$ given in Eq. 1, the relation $\vec{j} = \bar{\sigma}\vec{E}$ can be written as:

$$\begin{pmatrix} j_{a^*} \\ j_b \\ j_c \end{pmatrix} = \bar{\sigma} \begin{pmatrix} E_{a^*} \\ E_b \\ E_c \end{pmatrix} = \begin{pmatrix} \sigma_{a^*a^*}E_{a^*} + \sigma_{a^*c}E_c \\ \sigma_{bb}E_b \\ \sigma_{a^*c}E_{a^*} + \sigma_{cc}E_c \end{pmatrix} \quad (2)$$

in the a^*bc Cartesian coordinate system. This equation will be used next for the determination of the 2D conductivity tensor in terms of 3D conductivity tensor elements. The difference compared to isotropic materials can be seen in Eq. 2: the direction of \vec{E} can be different from the direction of the current \vec{j} , i. e. an out of plane electric field can exist for samples with in-plane current and the orientation of the sample compared to the reference system has to be considered.

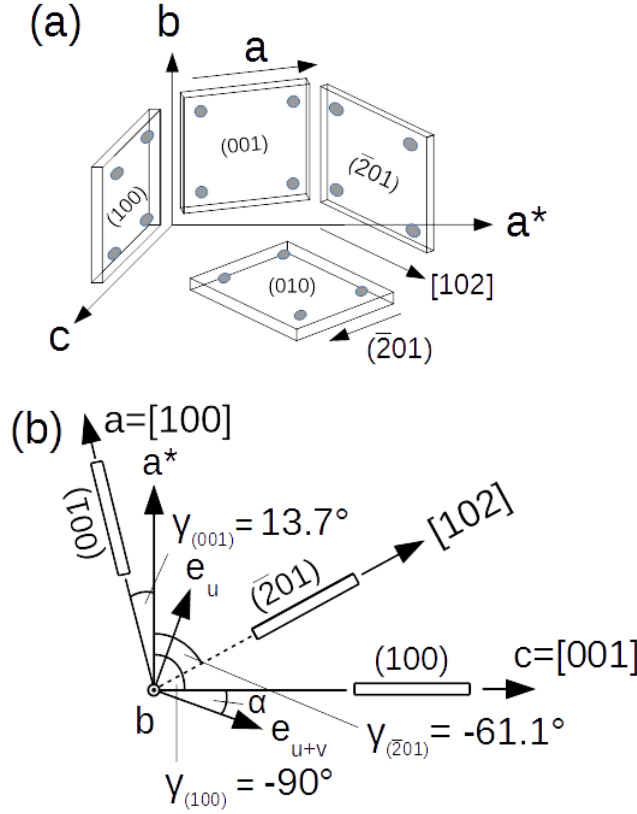


Figure 5: (a) Overview of the orientation of the samples. Three samples have one edge along the b -direction and the other edge is within the ac plane. (b) These three samples and the angles between them are shown in a projection onto the ac -plane. This sketch includes the room-temperature directions of minimum and maximum conductivity in the ac plane.

1. (100) orientation

For our (100)-surface samples ($=a^*$) with edges along $[010]=b$ and $[001]=c$, defining our Cartesian a^*bc reference system, the condition of zero current perpendicular to the surface ($j_{a^*} = j_{\perp} = 0$), can be applied to Eq. 2:

$$0 = \sigma_{a^*a^*}E_{a^*} + \sigma_{a^*c}E_c \quad (3)$$

which is equivalent to fixing the electric field perpendicular to the surface to

$$E_{a^*} = -\frac{\sigma_{a^*c}E_c}{\sigma_{a^*a^*}} \quad (4)$$

Using Eq. 2 and Eq. 3:

$$\begin{aligned} \begin{pmatrix} j_{a^*} \\ j_b \\ j_c \end{pmatrix} &= \begin{pmatrix} \sigma_{a^*a^*}(-\frac{\sigma_{a^*c}E_c}{\sigma_{a^*a^*}}) + \sigma_{a^*c}E_c \\ \sigma_{bb}E_b \\ \sigma_{a^*c}(-\frac{\sigma_{a^*c}E_c}{\sigma_{a^*a^*}}) + \sigma_{cc}E_c \end{pmatrix} \\ &= \begin{pmatrix} 0 \\ \sigma_{bb}E_b \\ (\sigma_{cc} - \frac{\sigma_{a^*c}^2}{\sigma_{a^*a^*}})E_c \end{pmatrix} \end{aligned} \quad (5)$$

which can be rewritten to

$$\begin{pmatrix} j_{a^*} \\ j_b \\ j_c \end{pmatrix} = \begin{pmatrix} 0 & 0 & 0 \\ 0 & \sigma_{bb} & 0 \\ 0 & 0 & \sigma_{cc} - \frac{\sigma_{a^*c}^2}{\sigma_{a^*a^*}} \end{pmatrix} \begin{pmatrix} E_{a^*} \\ E_b \\ E_c \end{pmatrix}. \quad (6)$$

The 2D tensor in the coordinate system of the sample edges, the axes b and c , is now given by the bc -components of the conductivity tensor in Eq. 6:

$$\bar{\sigma}^{bc} = \begin{pmatrix} \sigma_{bb} & 0 \\ 0 & \sigma_{cc} - \frac{\sigma_{a^*c}^2}{\sigma_{a^*a^*}} \end{pmatrix} \quad (7)$$

The experimentally determined value of the conductivity anisotropy of one sample can now be given as the ratio of the diagonal elements in Eq. 7:

$$A_{\sigma}^{(100)} = \frac{\sigma_{cc} - \frac{\sigma_{a^*c}^2}{\sigma_{a^*a^*}}}{\sigma_{bb}} \quad (8)$$

2. (001) orientation

The same derivation as for the (100)-surface samples can be done for (001)-surface samples ($=c^*$) (edges along $[100]=a$ and $[010]=b$), but in the abc^* Cartesian coordinate system. The angle between the a^*bc and abc^* Cartesian coordinate systems is 13.7° around the b -axis ($=$ angle between a and a^* as well as c^* and c).

$$\bar{\sigma}^{ab} = \begin{pmatrix} \sigma_{aa} - \frac{\sigma_{ac^*}^2}{\sigma_{c^*c^*}} & 0 \\ 0 & \sigma_{bb} \end{pmatrix} \quad (9)$$

whose components consist of conductivity components of the 3D conductivity tensor written in the abc^* system. Hence, the experimentally determined value of the conductivity anisotropy is the ratio of the diagonal elements in Eq. 9:

$$A_{\sigma}^{(001)} = \frac{\sigma_{aa} - \frac{\sigma_{ac^*}^2}{\sigma_{c^*c^*}}}{\sigma_{bb}}. \quad (10)$$

To relate the abc^* -system tensor components to the a^*bc -system tensor components of Eq. 1, a rotation has to be applied to the tensor.

$$\bar{\sigma}_{rot} = R_{\alpha} \bar{\sigma} R_{\alpha}^{-1} \quad (11)$$

where the rotated conductivity tensor σ_{rot} follows a unitary transformation using the rotation matrix for a rotation around the b -axis

$$R_{\alpha} = \begin{pmatrix} \cos(\alpha) & 0 & \sin(\alpha) \\ 0 & 1 & 0 \\ -\sin(\alpha) & 0 & \cos(\alpha) \end{pmatrix} \quad (12)$$

The transformation described by Eq. 11 can be derived by writing the relation $\vec{j} = \bar{\sigma} \vec{E}$ before and after applying a rotation:

$$\vec{j}_{rot} = R_{\alpha} \vec{j} = R_{\alpha} \bar{\sigma} \vec{E} = R_{\alpha} \bar{\sigma} R_{\alpha}^{-1} R_{\alpha} \vec{E} = \bar{\sigma}_{rot} \vec{E}_{rot} \quad (13)$$

To rotate the coordinate system by a certain angle, both vectors and matrices have to be rotated by the negative value of that angle. To transform a tensor from the abc^* -system to the a^*bc -system, a rotation around the b -axis of $\gamma_{(001)} = -13.7^\circ$ has to be applied to the tensor. Using this rotation, the abc^* tensor elements can be expressed in terms of the a^*bc tensor elements:

$$\begin{aligned} \sigma_{aa} &= \sigma_{a^*a^*} \cos^2 \gamma_{(001)} - \sin(2\gamma_{(001)}) \sigma_{a^*c} \\ &\quad + \sigma_{cc} \sin^2 \gamma_{(001)} \end{aligned} \quad (14)$$

$$\begin{aligned} \sigma_{ac^*} &= \sin \gamma_{(001)} \cos \gamma_{(001)} \sigma_{a^*a^*} + \cos(2\gamma_{(001)}) \sigma_{a^*c} \\ &\quad - \sin \gamma_{(001)} \cos \gamma_{(001)} \sigma_{cc} \end{aligned} \quad (15)$$

$$\begin{aligned} \sigma_{c^*c^*} &= \sin^2 \gamma_{(001)} \sigma_{a^*a^*} + \sin(2\gamma_{(001)}) \sigma_{a^*c} \\ &\quad + \cos^2 \gamma_{(001)} \sigma_{cc} \end{aligned} \quad (16)$$

where σ_{bb} remains unchanged.

3. $(\bar{2}01)$ orientation

For $(\bar{2}01)$ -sample, the 2D conductivity tensor in the coordinate system can be derived like for the (100) - and the (001) -surface samples, but in the coordinate system of the sample edges $[010]$ and $[102]$. In that system, the two-dimensional conductivity tensor can be given as:

$$\bar{\sigma}^{[102],b} = \begin{pmatrix} \sigma_{[102][102]} - \frac{\sigma_{(\bar{2}01)[102]}^2}{\sigma_{(\bar{2}01)(\bar{2}01)}} & 0 \\ 0 & \sigma_{bb} \end{pmatrix} \quad (17)$$

Hence, the experimentally determined value of the conductivity anisotropy is the ratio of the diagonal elements in Eq. 17:

$$A_{\sigma}^{(\bar{2}01)} = \frac{\sigma_{[102][102]} - \frac{\sigma_{(\bar{2}01)[102]}^2}{\sigma_{(\bar{2}01)(\bar{2}01)}}}{\sigma_{bb}}. \quad (18)$$

Using a rotation of $\gamma_{(\bar{2}01)} = 61.1^\circ$ around the b -axis, the $[102]b(\bar{2}01)$ tensor elements can be expressed in terms of the a^*bc tensor elements in the same form as for the (001) -surface samples:

$$\begin{aligned} \sigma_{[102][102]} &= \cos^2 \gamma_{(\bar{2}01)} \sigma_{a^*a^*} - \sin(2\gamma_{(\bar{2}01)}) \sigma_{a^*c} \\ &\quad + \sin^2 \gamma_{(\bar{2}01)} \sigma_{cc} \end{aligned} \quad (19)$$

$$\begin{aligned} \sigma_{[102](\bar{2}01)} &= \sin \gamma_{(\bar{2}01)} \cos \gamma_{(\bar{2}01)} \sigma_{a^*a^*} + \cos(2\gamma_{(\bar{2}01)}) \sigma_{a^*c} \\ &\quad - \sin \gamma_{(\bar{2}01)} \cos \gamma_{(\bar{2}01)} \sigma_{cc} \end{aligned} \quad (20)$$

$$\begin{aligned} \sigma_{(\bar{2}01)(\bar{2}01)} &= \sin^2 \gamma_{(\bar{2}01)} \sigma_{a^*a^*} + \sin(2\gamma_{(\bar{2}01)}) \sigma_{a^*c} \\ &\quad + \cos^2 \gamma_{(\bar{2}01)} \sigma_{cc} \end{aligned} \quad (21)$$

where σ_{bb} again remains unchanged.

4. (010) orientation

For completeness we are giving the transformation for (010) -surface samples with edges along $[102]$ and $\perp [102]$ as well. The three-dimensional conductivity tensor from Eq. 1 can be directly rewritten into a two-dimensional Tensor in the a^*c -system by removing the second row and column:

$$\sigma^{a^*c} = \begin{pmatrix} \sigma_{a^*a^*} & \sigma_{a^*c} \\ \sigma_{a^*c} & \sigma_{cc} \end{pmatrix} \quad (22)$$

As the sample edges are along $[102]$ and $\perp [102]$, a rotation of about $\gamma_{(010)} = 61.1^\circ$ ($=\gamma_{(\bar{2}01)}$) around the b -axis has to be applied to get the conductivity tensor in the coordinate system of the sample edges:

$$\sigma^{[102],\perp[102]} = \begin{pmatrix} \sigma_{[102][102]} & \sigma_{[102],\perp[102]} \\ \sigma_{[102],\perp[102]} & \sigma_{\perp[102],\perp[102]} \end{pmatrix} \quad (23)$$

where:

$$\begin{aligned} \sigma_{[102][102]} &= \cos^2 \gamma_{(010)} \sigma_{a^*a^*} - \sin(2\gamma_{(010)}) \sigma_{a^*c} \\ &\quad + \sin^2 \gamma_{(010)} \sigma_{cc} \end{aligned} \quad (24)$$

$$\begin{aligned} \sigma_{[102],\perp[102]} &= \sin \gamma_{(010)} \cos \gamma_{(010)} \sigma_{a^*a^*} + \cos(2\gamma_{(010)}) \sigma_{a^*c} \\ &\quad - \sin \gamma_{(010)} \cos \gamma_{(010)} \sigma_{cc} \end{aligned} \quad (25)$$

$$\begin{aligned} \sigma_{\perp[102],\perp[102]} &= \sin^2 \gamma_{(010)} \sigma_{a^*a^*} + \sin(2\gamma_{(010)}) \sigma_{a^*c} \\ &\quad + \cos^2 \gamma_{(010)} \sigma_{cc}. \end{aligned} \quad (26)$$

F. Reconstructing the 3-dimensional conductivity tensor

The 3D conductivity tensor has four independent elements (compare Eq. 1). Measurements of the 2D in-plane conductivity anisotropy of three differently oriented samples are thus sufficient to characterize the 3D conductivity anisotropy, as the tensor components can be normalized to one of the components. The (100) , the (001) and the $(\bar{2}01)$ surface samples all share one edge along the b -direction and the other one in the ac plane (visualized in Fig. 5(a)). Thus, the measured anisotropies (Eqs. 8, 10, 18) are ratios of ac -plane conductivities and σ_{bb} .

The 3D conductivity tensor Eq. 1 can be diagonalized by rotating the a^*bc coordinates system by an angle α around the b -axis into an arbitrary coordinate system, whose axes in the ac -plane are given by the directions e_u and e_{u+v} of minimum and maximum conductivity u and $(u+v)$, respectively, in the ac -plane (as illustrated in Fig. 5(b)):

$$\sigma^{min,max} = \begin{pmatrix} u & 0 & 0 \\ 0 & \sigma_{bb} & 0 \\ 0 & 0 & u+v \end{pmatrix}. \quad (27)$$

Conversely, $\sigma^{min,max}$ can be expressed in the a^*bc system by a rotation of the coordinate system of $-\alpha$ around the b -

axis:

$$\begin{aligned}\sigma^{a*bc} &= \begin{pmatrix} \sigma_{a^*a^*} & 0 & \sigma_{a^*c} \\ 0 & \sigma_{bb} & 0 \\ \sigma_{a^*bc} & 0 & \sigma_{cc} \end{pmatrix} \\ &= \begin{pmatrix} u + v\sin^2\alpha & 0 & v\sin\alpha\cos\alpha \\ 0 & \sigma_{bb} & 0 \\ v\sin\alpha\cos\alpha & 0 & u + v\cos^2\alpha \end{pmatrix}. \quad (28)\end{aligned}$$

Using the relation between the $e_u b e_{u+v}$ and the a^*bc coordinate system conductivity values in Eq. 28, Eq. 8 can be rewritten as

$$A_\sigma^{(100)} = \frac{(u + v\cos^2\alpha) - \frac{(v\sin\alpha\cos\alpha)^2}{(u + v\sin^2\alpha)}}{\sigma_{bb}} \quad (29)$$

which is equivalent to

$$A_\sigma = \frac{u/\sigma_{bb} + v/\sigma_{bb}}{1 + \frac{v}{u}\sin^2(\alpha)} \quad (30)$$

Using γ , the angle describing the orientation of the sample edges in the a^*bc coordinate system (see Fig. 5(b)), that equation can be rewritten to

$$\frac{u/\sigma_{bb} + v/\sigma_{bb}}{1 + \frac{v}{u}\cos^2(\alpha - \gamma)} = A_\sigma \quad (31)$$

with $\gamma_{(100)} = -90^\circ$. The same can be done for the (001) and the $(\bar{2}01)$ -surface samples, taking Eqs. 10 and 18 to arrive at the same equation. The rotation between the system of the sample edges and the a^*bc -system (Eqs. 14 to 16 and 19 to 21) is expressed in γ in each case. For our oriented samples, $\gamma_{(001)} = 13.7^\circ$ and $\gamma_{(\bar{2}01)} = -61.1^\circ$.

For these three sample orientations α , u/σ_{bb} , and v/σ_{bb} are the same, and can thus be determined by solving the resulting system of the three coupled Eqs. 31 numerically using the experimentally obtained A_σ and known γ . The conductivity tensor in the a^*c system can then be readily calculated from these results by equating the tensor components in Eq. 28.

III. RESULTS AND DISCUSSION

A. Room temperature results

The measured value of the 2D conductivity anisotropy at room temperature, together with their relation to the three-dimensional conductivity tensor $\bar{\sigma}$ by Eqs. 7, 9, and 17 are summarized in Tab. V. For all samples, except G100c containing extended defects, a fairly isotropic in-plane conductivity was observed at room temperature with deviation of the conductivity anisotropy from unity of below 5% and even below 1% for three of these samples. Theory suggests a dependence of transport anisotropy on electron concentration or prevalent scattering mechanism (see Refs. [23, 24] and Tab. I). We are thus using the data of samples G100a and G001a, which have very similar electron concentrations, and that of

Table V: Values of the measured 2D conductivity anisotropy A at room temperature for different samples. The values were derived from comparing the measured van der Pauw anisotropy A_{vdP} to finite element simulations (see Tab. III). As the off-diagonal element is much smaller than the diagonal elements, the given values are an approximation for the ratio of the conductivity along one side of the sample (c -axis, a -axis, $[1\ 0\ 2]$) and the other (b -axis).

Sample name	2D anisotropy (3D Tensor elements)	2D anisotropy value
G100a	$\frac{\sigma_{cc} - \frac{\sigma_{ac}^2}{\sigma_{aa}}}{\sigma_{bb}}$	0.960 ± 0.01
G100b	$\frac{\sigma_{cc} - \frac{\sigma_{ac}^2}{\sigma_{aa}}}{\sigma_{bb}}$	1.000 ± 0.02
G100c (extended defects)	$\frac{\sigma_{cc} - \frac{\sigma_{ac}^2}{\sigma_{aa}}}{\sigma_{bb}}$	0.768 ± 0.01
G001a	$\frac{\sigma_{aa} - \frac{\sigma_{ac}^2}{\sigma_{cc}}}{\sigma_{bb}}$	1.000 ± 0.01
G-201a	$\frac{\sigma_{[102]} - \frac{\sigma_{[102](\bar{2}01)}}{\sigma_{(\bar{2}01)}}}{\sigma_{bb}}$	0.995 ± 0.01

G-201a to obtain the conductivity tensor Eq. 1 in the a^*bc reference system by solving the system of coupled Eqs. 31. The resulting tensor (normalized to the conductivity in b -direction) at room temperature and an electron concentration of $n = (3.5 \pm 1) \times 10^{17} \text{ cm}^{-3}$ is:

$$\bar{\sigma}/\sigma_{bb}(T = 300\text{K}) = \begin{pmatrix} 1.02 \pm 0.02 & 0 & 0.03 \pm 0.03 \\ 0 & 1 & 0 \\ 0.03 \pm 0.03 & 0 & 0.96 \pm 0.02 \end{pmatrix}. \quad (32)$$

Our results indicate a small anisotropy of the conductivity with $\sigma_{a^*a^*}$ and σ_{cc} being few % higher and lower than σ_{bb} , respectively, and the non-diagonal elements σ_{a^*c} amounting to no more than a few % of σ_{bb} .

To analyze the anisotropies of the scattering time, the conductivity tensor can be compared to an effective mass tensor. The tensor taken from [25], which Furthmuller et al. calculated by first principles, can be rotated to the a^*bc reference system and normalized to m^* along the b -axis:

$$\bar{m}^*/m_{bb}^* = \begin{pmatrix} 1.009 & 0 & -0.001 \\ 0 & 1 & 0 \\ -0.001 & 0 & 0.973 \end{pmatrix} \quad (33)$$

As the conductivity and the effective mass are close to isotropic, the overall scattering time at room temperature is quite isotropic as well. Using the relation $\bar{\sigma} = e \frac{\bar{\tau}}{m^*}$, the results from Eq. 32, and the effective mass tensor from [25], the τ -tensor normalized to τ_{bb} , can be calculated to be:

$$\tau/\tau_{bb} = \begin{pmatrix} 1.03 \pm 0.02 & 0 & 0.03 \pm 0.03 \\ 0 & 1 & 0 \\ 0.03 \pm 0.03 & 0 & 0.93 \pm 0.02 \end{pmatrix} \quad (34)$$

at room temperature with $\tau_{a^*a^*}$ being 10% higher than τ_{cc} .

B. Temperature dependence and scattering mechanisms

The temperature dependence between 50 K and 380 K of measured 2D-conductivity anisotropies A in the coordinate

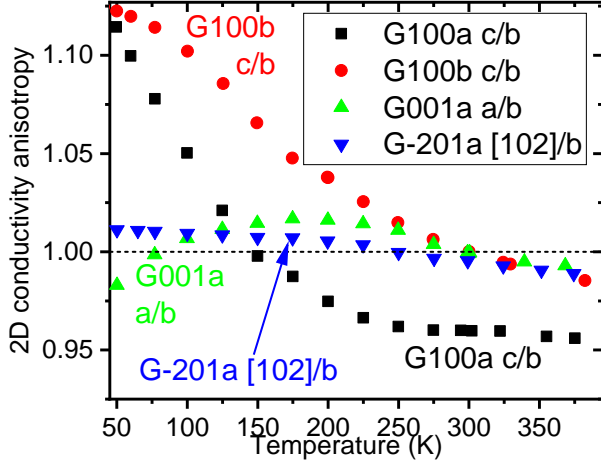


Figure 6: Temperature-dependent 2D conductivity anisotropy A for samples with different surface orientations. The in-plane directions of the sample edges that result in the conductivity anisotropy, e.g. “ c/b ” resulting in $A = \sigma_{\parallel c}/\sigma_{\parallel b}$, are given with the sample name. The dashed line denotes completely isotropic in-plane conductivity.

system of the sample edges are shown in Fig. 6. Samples G001a and G-201a remain completely isotropic within 2% and 1%, respectively, for the entire temperature range. For the temperature decreasing from ≈ 370 K to 50 K both, G100a and G100b, clearly show an increasing anisotropy ($A = \sigma_{\parallel c}/\sigma_{\parallel b}$) from 0.96 and 0.99 to 1.11 and 1.12, respectively. A deviation of A from unity of less than 5% can be seen for temperatures between 175 K and 380 K for all samples. These results suggest a rather isotropic conductivity at application-relevant (high) temperatures.

Next, we will address the impact of scattering mechanism on transport anisotropy. The electron mobility in β -Ga₂O₃ free from extended defects is mainly limited by polar longitudinal optical phonon scattering (PLOPS) and ionized impurity scattering (IIS) at fixed ionized point charges[23, 28]. With increasing temperature the electron mobility limited by PLOPS or IIS decreases or increases, respectively, and higher ionized point charge concentrations (including dopants, compensating dopants, or point defects) decrease the IIS-limited mobility[28]. To identify the dominant scattering mechanisms (PLOPS or IIS) for all samples we compare our measured temperature dependent mobilities and electron concentrations shown in Fig. 7 to modeled- and reference data from Ref. [28]: The high mobility at $T = 300$ K which strongly increases with decreasing temperature in samples G100a and G001a (Fig. 7, left) indicates dominant PLOPS at $T \gtrsim 200$ K. Consistent with this assignment, the intermediate electron concentrations of these samples (Fig. 7, right) corresponds to a donor concentration that is low enough (and not significantly compensated) to be clearly in the regime of dominant PLOPS (cf. Ref. [28]). Due to the small off-diagonal element $\sigma_{a^*c}/\sigma_{bb}$, the experimentally obtained conductivity anisotropies of G100a and G001a shown in Fig. 6, are good approximations of $\sigma_{cc}/\sigma_{bb} \approx 0.96$ and $\sigma_{aa}/\sigma_{bb} \approx 1.00$ for PLOPS. This fairly isotropic PLOPS is in fair agreement with the theoretically predicted

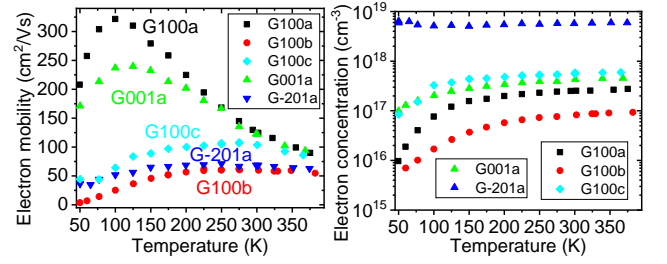


Figure 7: Average Hall mobility (left) and electron concentration (right) as a function of temperature for various sample orientations. Measured values were corrected for geometry effects of non-edge contact placement and finite contact size (see Tab. IV for correction factors).

$\sigma_{c^*c^*}/\sigma_{bb} \approx 1.02$ of Ref. [23] but significantly contrasts the predicted stronger anisotropy of $\sigma_{c^*c^*}/\sigma_{bb} \approx 0.64$ of Ref. [24] and $\sigma_{aa}/\sigma_{bb} \approx 0.84$ of Ref. [23] for comparable electron concentrations. (We note that a and a^* as well as c^* and c are different from each other. The rotation from the abc^* -system (used in the theory Refs. [23, 24]) to the a^*bc -system (used by us) by 13.7° , however, is small enough to grant quantitative comparison of the anisotropies along these directions.) In marked contrast, the mobilities of G-201a and G100b are significantly lower and show only a weak temperature dependence at $T \gtrsim 200$ K, indicating strong IIS. The high, degenerate electron concentration shown in Fig. 7, right for G-201a, implying a high donor concentration, corroborates strong IIS, whereas strong IIS in G100b with rather low electron concentration can only be explained by compensation. Our experimental results further limit the uncertainty, in particular with regard to the directions, from a maximum 40% and 10% deviation from the isotropic case experimentally determined by optical Hall effect measurements of samples with high donor concentration[22] and estimated theoretically for IIS[23], respectively: Comparing G100b (strong IIS) to G100a (weaker IIS) we find the anisotropy $A = \sigma_{\parallel c}/\sigma_{\parallel b} \approx \sigma_{cc}/\sigma_{bb}$ to be systematically higher for G100b (see in Fig. 6). This behavior is in qualitative agreement with an increase of A for G100a with decreasing temperature, i.e. with decreasing PLOPS and increasing IIS. At $T \lesssim 100$ K decreasing mobility with decreasing temperature indicates dominant IIS in all samples. Under these conditions the anisotropy of G100a,b reaches $\sigma_{cc}/\sigma_{bb} \approx 1.12$ whereas $\sigma_{[102]}/\sigma_{bb}$ of G-201a and σ_{aa}/σ_{bb} of G001a remain within 1% and 2% around unity. These results indicate fairly isotropic IIS. The systematically higher conductivity in the c -direction compared to the almost equal conductivities in the a - and b -direction is likely related to higher dielectric constant for the c -direction compared to the almost equal dielectric constants for directions perpendicular to c . [15, 16]

Neglecting potentially different anisotropies associated to different scattering mechanisms (in samples G-201a compared to G100a and G001a) we can determine the temperature-dependent conductivity tensor Eq. 1 normalized to the conductivity in b -direction, $\bar{\sigma}/\sigma_{bb}$, by numerically solving Eq. 31 with the data from our experimentally temperature-

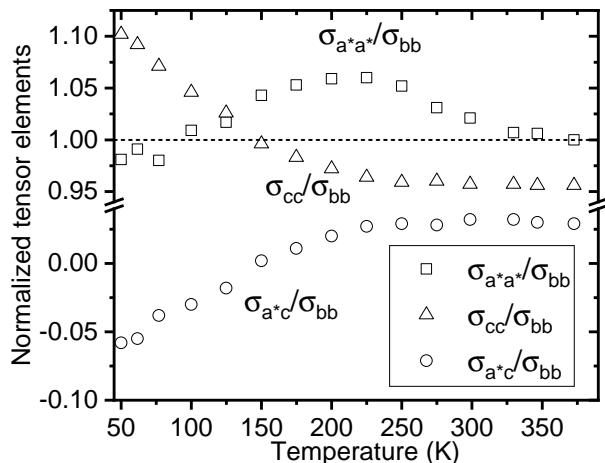


Figure 8: Visualization of the temperature-dependent 3D conductivity tensor elements of $\beta\text{-Ga}_2\text{O}_3$ normalized to the conductivity in b -direction, σ_{bb} .

dependent 2D conductivity anisotropies of G100a, G001a, and G-201a. The resulting temperature dependent tensor components are shown in Fig. 8.

C. Anisotropy by extended defects

Large conductivity anisotropies with significantly higher conductivity in the b than in the c -direction have been identified in sample G100c, which contains low-angle grain boundaries oriented approximately along the b -direction (see and Fig. 2). In this sample, the room temperature conductivity anisotropy $\sigma_{cc}/\sigma_{bb} \approx 0.77$ (shown in Tab. V) is much stronger than that of the comparable high-quality samples G100a and G100b. A qualitatively similar behavior with $\sigma_{cc}/\sigma_{bb} \approx 0.06$ and $\sigma_{cc}/\sigma_{bb} \approx 0.5$ at room temperature has been observed in $\beta\text{-Ga}_2\text{O}_3$ (100) bulk samples of unknown structural quality[10] and MOVPE layers containing a high density of incoherent twin boundaries oriented along the b -direction.[19] Planar defects, such as twin- or grain boundaries are typically associated with energy barriers that impede electron transport across, explaining the relatively lower conductivity along the c -direction for G100c[33, 34]. For convenience we plot the temperature dependence of the inverse anisotropy, σ_{bb}/σ_{cc} , for sample G100c in Fig. 9. A strong increase of anisotropy with decreasing temperature from $\sigma_{bb}/\sigma_{cc} = 1.14$ at $T = 360\text{K}$ to $\sigma_{bb}/\sigma_{cc} > 20$ at $T = 50\text{K}$ is observed. It follows an activated behavior and the activation energy for the conductivity in the c direction (across the barriers) for $T > 100\text{K}$ was calculated according to $\sigma_{[001]} = \sigma_0 e^{-\frac{E_a}{kT}}$ to be $E_A = (38 \pm 2)\text{ meV}$. (We note that the increasing anisotropy σ_{cc}/σ_{bb} with decreasing temperature in samples G100a and G100b cannot be related to such extended defects as it is inverse to the increasing σ_{bb}/σ_{cc} of G100c.)

Figure 10 shows the mobility in the direction parallel and perpendicular to the low-angle grain boundary defects in sample G100c. Parallel to the defects, the mobility is only slightly

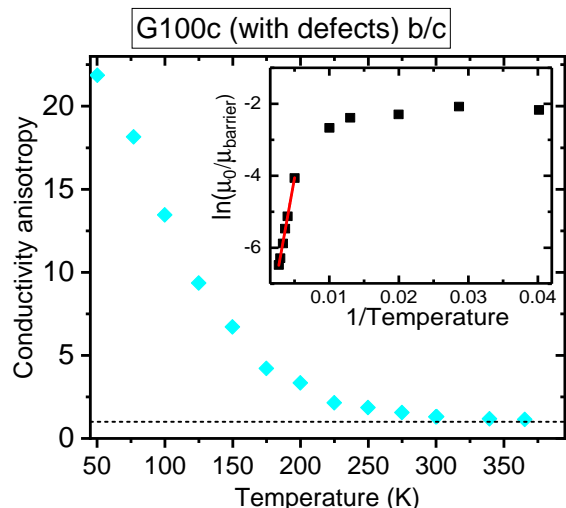


Figure 9: Conductivity anisotropy of sample G100c containing visible defects (low-angle grain boundaries along the b -direction). The dashed line denotes completely isotropic in-plane conductivity. The inset shows an Arrhenius plot of the barrier-related mobility, the fit between 200 K and 365 K results in an activation energy of $38 \pm 2\text{ meV}$.

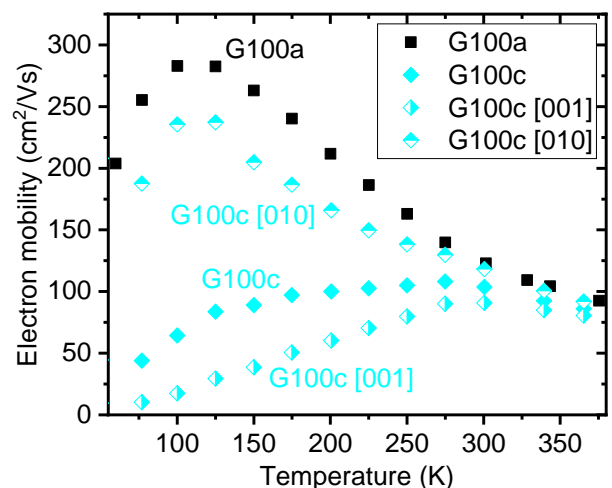


Figure 10: Temperature-dependent Hall mobility for sample G100c containing low-angle grain boundaries along the b -direction. Cyan rhombs: average mobility and mobility along and perpendicular to the defects. Black squares: mobility of the sample G100a without these defects for comparison.

lower than that of a comparable sample without these defects, G100a, whereas it is drastically reduced perpendicular to the defects, especially at low temperatures. Above room temperature, however, the mobilities in both direction coincide and decrease with increasing temperature as expected for phonon-limited transport, indicating a negligible effect of the grain boundaries. Assuming the mobility μ within the grains to be isotropic the total mobility perpendicular to the defects ([001]-direction), μ_{\perp} , is reduced due to the activated, barrier-related

mobility μ_{barrier} :

$$\frac{1}{\mu_{\perp}} = \frac{1}{\mu} + \frac{1}{\mu_{\text{barrier}}} \quad (35)$$

As $A_{\sigma} \approx \frac{\sigma_{bb}}{\sigma_{cc}} \approx \mu/\mu_{\perp}$:

$$\mu_{\text{barrier}} = \frac{\mu}{A_{\sigma} - 1} = \mu_0 e^{\frac{E_a}{kT}} \quad (36)$$

using this equation, the activation energy for the transport across the barriers is $E_A = (93 \pm 2)$ meV for temperatures between $T = 200$ K and $T = 365$ K (see inset of Fig. 9). Interestingly, this barrier is orders of magnitude higher than that found at low-angle grain boundaries of bulk SnO_2 [31], which might also explain the difficulties in realizing conductive, non-single crystalline $\beta\text{-Ga}_2\text{O}_3$ films.

IV. SUMMARY AND CONCLUSION

Using van der Pauw measurements with well-defined contact geometry and careful FEM modeling of the structures, the anisotropy of the electrical conductivity in high-quality bulk $\beta\text{-Ga}_2\text{O}_3$ wafers with different surface orientation was precisely determined.

Most importantly, fairly isotropic behavior with conductivity ratios of different directions between 0.96 ± 0.01 and 1.06 ± 0.02 at temperatures between 150 K and 375 K were found at electron concentrations on the order of 10^{17} cm^{-3} . Based on the extracted anisotropies, the ratio of the non-zero elements of the conductivity tensor were determined. Comparison to the effective mass tensor indicates that the transport anisotropy is strongly influenced by the scattering times of anisotropic scattering mechanisms. Close inspection of the temperature-dependent electron mobility between 50 and 375 K allowed us to distinguish dominant polar longitudinal optical phonon scattering (PLOPS) from dominant ionized impurity scattering (IIS): Irrespective of scattering mechanism, the conductivities in the a and b directions agree within 2%. The ratio of the conductivities along the c and b direction, however, is 0.96 ± 0.01 for PLOPS and increases up to

1.12 for IIS. The $a - b$ isotropy and $c - b$ anisotropy of IIS may be related to the corresponding anisotropy of the dielectric constant of $\beta\text{-Ga}_2\text{O}_3$. [15, 16] We experimentally demonstrate that significantly higher anisotropies can be caused by extended structural defects in the form of low-angle grain boundaries whose barriers were found to be multiple 10 meV high.

Since the inherent electrical conductivity tensor of $\beta\text{-Ga}_2\text{O}_3$ can be considered fairly isotropic for practical applications no particular transport direction is advantageous for increasing the electron mobility for optimum performance of transport-based electronic devices, such as transistors. Conductivity anisotropies of more than a few percent, as found in Refs. [10, 20, 21] are likely not intrinsic, but rather related to experimental artifacts or to extrinsic causes, such as extended structural defects like incoherent twin boundaries [19] or grain boundaries. The van der Pauw method used here is an experimentally straightforward method to measure the in-plane transport anisotropy of a given sample. We suggest to use the conductivity anisotropy of a sample as a quality indicator to indicate extended defects oriented along a certain crystallographic direction.

Most of the conductivity anisotropies predicted by first principles [23, 24] are significantly larger than those experimentally found in this work. Their predicted dependence on electron concentration [23, 24] requires further experimental investigation, in particular towards electron concentrations above 10^{19} cm^{-3} .

Acknowledgments

We thank F. Henschke for preparing the shadow mask, S. Rauwerdink, W. Seidel, and W. Anders for lithography and contact deposition, A. Riedel for wire bonding, as well as K. Irmscher for critically reading the manuscript. This work was performed in the framework of GraFOx, a Leibniz-ScienceCampus partially funded by the Leibniz association. C. G. gratefully acknowledges financial support by the Leibniz Association.

-
- [1] M. Higashiwaki, A. Kuramata, H. Murakami, and Y. Kumagai, *Journal of Physics D: Applied Physics* **50**, 333002 (2017), URL <https://doi.org/10.1088/1361-6463/aa7aff>.
 [2] M. Higashiwaki and G. H. Jessen, *Applied Physics Letters* **112**, 060401 (2018), URL <https://doi.org/10.1063/1.5017845>.
 [3] T. Oshima, T. Okuno, and S. Fujita, *Japanese Journal Of Applied Physics Part 1-Regular Papers Brief Communications & Review Papers* **46**, 7217 (2007), URL <https://doi.org/10.1143/JJAP.46.7217>.
 [4] U. Lampe, M. Fleischer, and H. Meixner, *Sensors and Actuators B: Chemical* **17**, 187 (1994), ISSN 0925-4005, URL [https://doi.org/10.1016/0925-4005\(93\)00880-8](https://doi.org/10.1016/0925-4005(93)00880-8).
 [5] S. Geller, *J. Chem. Phys.* **33**, 676 (1960), URL <https://doi.org/10.1063/1.1731237>.

- doi.org/10.1063/1.1731237.
 [6] Z. Guo, A. Verma, X. Wu, F. Sun, A. Hickman, T. Masui, A. Kuramata, M. Higashiwaki, D. Jena, and T. Luo, *Applied Physics Letters* **106**, 111909 (2015), URL <https://doi.org/10.1063/1.4916078>.
 [7] M. D. Santia, N. Tandon, and J. D. Albrecht, *Applied Physics Letters* **107**, 041907 (2015), URL <https://doi.org/10.1063/1.4927742>.
 [8] M. Handwerg, R. Mitdank, Z. Galazka, and S. F. Fischer, *Semiconductor Science and Technology* **31**, 125006 (2016), URL <https://doi.org/10.1088/0268-1242/31/12/125006>.
 [9] C. Sturm, J. Furthmüller, F. Bechstedt, R. Schmidt-Grund, and M. Grundmann, *APL Mater.* **3**, 106106 (2015), URL <https://doi.org/10.1063/1.4916078>.

- //doi.org/10.1063/1.4934705.
- [10] N. Ueda, H. Hosono, R. Waseda, and H. Kawazoe, *Applied Physics Letters* **71**, 933 (1997), URL <https://doi.org/10.1063/1.119693>.
- [11] T. Onuma, S. Saito, K. Sasaki, T. Masui, T. Yamaguchi, T. Honda, and M. Higashiwaki, *Japanese Journal of Applied Physics* **54**, 112601 (2015), URL <https://doi.org/10.7567/JJAP.54.112601>.
- [12] H. He, R. Orlando, M. A. Blanco, R. Pandey, E. Amzallag, I. Baraille, and M. Rérat, *Phys. Rev. B* **74**, 195123 (2006), URL <https://doi.org/10.1103/PhysRevB.74.195123>.
- [13] B. Liu, M. Gu, and X. Liu, *Applied Physics Letters* **91**, 172102 (2007), URL <https://doi.org/10.1063/1.2800792>.
- [14] M. Schubert, R. Korlacki, S. Knight, T. Hofmann, S. Schöche, V. Darakchieva, E. Janzén, B. Monemar, D. Gogova, Q.-T. Thieu, et al., *Phys. Rev. B* **93**, 125209 (2016), URL <https://doi.org/10.1103/PhysRevB.93.125209>.
- [15] A. Fiedler, R. Schewski, Z. Galazka, and K. Irmscher, *ECS Journal of Solid State Science and Technology* **8**, Q3083 (2019), <http://jss.ecsdl.org/content/8/7/Q3083.full.pdf+html>, URL <https://doi.org/10.1149/2.0201907jss>.
- [16] K. Ghosh and U. Singiseti, *Applied Physics Letters* **109**, 072102 (2016), <https://doi.org/10.1063/1.4961308>, URL <https://doi.org/10.1063/1.4961308>.
- [17] K. Irmscher, Z. Galazka, M. Pietsch, R. Uecker, and R. Fornari, *Journal of Applied Physics* **110**, 063720 (pages 7) (2011), URL <https://doi.org/10.1063/1.3642962>.
- [18] O. Bierwagen, R. Pomraenke, S. Eilers, and W. T. Masselink, *Physical Review B* **70**, 165307 (2004), URL <https://doi.org/10.1103/PhysRevB.70.165307>.
- [19] A. Fiedler, R. Schewski, M. Baldini, Z. Galazka, G. Wagner, M. Albrecht, and K. Irmscher, *Journal of Applied Physics* **122**, 165701 (2017), <http://dx.doi.org/10.1063/1.4993748>, URL <https://doi.org/10.1063/1.4993748>.
- [20] E. G. Villora, K. Shimamura, Y. Yoshikawa, K. Aoki, and N. Ichinose, *Journal of Crystal Growth* **270**, 420 (2004), URL <https://doi.org/10.1016/j.jcrysgro.2004.06.027>.
- [21] M. H. Wong, K. Sasaki, A. Kuramata, S. Yamakoshi, and M. Higashiwaki, *Japanese Journal of Applied Physics* **55**, 1202B9 (2016), URL <https://doi.org/10.7567/JJAP.55.1202B9>.
- [22] S. Knight, A. Mock, R. Korlacki, V. Darakchieva, B. Monemar, Y. Kumagai, K. Goto, M. Higashiwaki, and M. Schubert, *Applied Physics Letters* **112**, 012103 (2018), URL <https://doi.org/10.1063/1.5011192>.
- [23] Y. Kang, K. Krishnaswamy, H. Peelaers, and C. G. V. de Walle, *Journal of Physics: Condensed Matter* **29**, 234001 (2017), URL <https://doi.org/10.1088/1361-648X/aa6f66>.
- [24] K. Ghosh and U. Singiseti, *Journal of Materials Research* **32**, 4142 (2017), URL <https://doi.org/10.1557/jmr.2017.398>.
- [25] J. Furthmüller and F. Bechstedt, *Phys. Rev. B* **93**, 115204 (2016), URL <https://doi.org/10.1103/PhysRevB.93.115204>.
- [26] H. Peelaers and C. G. Van de Walle, *physica status solidi (b)* **252**, 828 (2015), ISSN 1521-3951, URL <https://doi.org/10.1002/pssb.201451551>.
- [27] K. Yamaguchi, *Solide State Commun.* **131**, 739 (2004), URL <https://doi.org/10.1016/j.ssc.2004.07.030>.
- [28] N. Ma, N. Tanen, A. Verma, Z. Guo, T. Luo, H. G. Xing, and D. Jena, *Applied Physics Letters* **109**, 212101 (2016), URL <https://doi.org/10.1063/1.4968550>.
- [29] Z. Galazka, K. Irmscher, R. Uecker, R. Bertram, M. Pietsch, A. Kwasniewski, M. Naumann, T. Schulz, R. Schewski, D. Klimm, et al., *Journal of Crystal Growth* **404**, 184 (2014), ISSN 0022-0248, URL <https://doi.org/10.1016/j.jcrysgro.2014.07.021>.
- [30] A. Kuramata, K. Koshi, S. Watanabe, Y. Yamaoka, T. Masui, and S. Yamakoshi, *Japanese Journal of Applied Physics* **55**, 1202A2 (2016), URL <https://doi.org/10.7567/JJAP.55.1202A2>.
- [31] O. Bierwagen and Z. Galazka, *Applied Physics Letters* **112**, 092105 (2018), URL <https://doi.org/10.1063/1.5018983>.
- [32] A. Parisini and R. Fornari, *Semiconductor Science and Technology* **31**, 035023 (2016), URL <https://doi.org/10.1088/0268-1242/31/3/035023>.
- [33] J. Y. W. Seto, *Journal of Applied Physics* **46**, 5247 (1975), URL <https://doi.org/10.1063/1.321593>.
- [34] J. W. Orton and M. J. Powell, *Reports on Progress in Physics* **43**, 1263 (1980), URL <https://doi.org/10.1088/0034-4885/43/11/001>.